

Phase-field study of three-dimensional steady-state growth shapes in directional solidification

Sebastian Gurevich and Alain Karma

Department of Physics and Center for Interdisciplinary Research on Complex Systems, Northeastern University, Boston, Massachusetts 02115, USA

Mathis Plapp

Physique de la Matière Condensée, Ecole Polytechnique, CNRS, 91128 Palaiseau, France

Rohit Trivedi

Department of Materials Science and Engineering, Iowa State University, Ames, Iowa 50010, USA

(Received 31 July 2009; published 14 January 2010)

We use a quantitative phase-field approach to study directional solidification in various three-dimensional geometries for realistic parameters of a transparent binary alloy. The geometries are designed to study the steady-state growth of spatially extended hexagonal arrays, linear arrays in thin samples, and axisymmetric shapes constrained in a tube. As a basis to address issues of dynamical pattern selection, the phase-field simulations are specifically geared to identify ranges of primary spacings for the formation of the classically observed “fingers” (deep cells) with blunt tips and “needles” with parabolic tips. Three distinct growth regimes are identified that include a low-velocity regime with only fingers forming, a second intermediate-velocity regime characterized by coexistence of fingers and needles that exist on separate branches of steady-state growth solutions for small and large spacings, respectively, and a third high-velocity regime where those two branches merge into a single one. Along the latter, the growth shape changes continuously from fingerlike to needlelike with increasing spacing. These regimes are strongly influenced by crystalline anisotropy with the third regime extending to lower velocity for larger anisotropy. Remarkably, however, steady-state shapes and tip undercoolings are only weakly dependent on the growth geometry. Those results are used to test existing theories of directional finger growth as well as to interpret the hysteretic nature of the cell-to-dendrite transition.

DOI: [10.1103/PhysRevE.81.011603](https://doi.org/10.1103/PhysRevE.81.011603)

PACS number(s): 68.08.–p, 81.30.Fb, 05.70.Ln, 64.70.D–

I. INTRODUCTION

The directional solidification of dilute binary alloys can produce a large variety of complex interfacial patterns. This phenomenon has been extensively studied both because of its metallurgical importance [1,2] and because it can be used as a model system for fundamental studies of pattern formation in spatially extended systems. In the typical small growth rate regime probed experimentally, the solid-liquid interface is to a good approximation in local thermodynamic equilibrium. In this regime, the emergence of cellular or dendritic array patterns results primarily from the interplay of a morphological instability driven by the diffusive transport of solute and the stabilizing effect of surface tension.

After the planar solid-liquid interface becomes unstable above a critical pulling speed v_c , typically observed directional solidification patterns include cells (round, fingerlike shapes) and dendrites (needle crystals decorated with side-branches). A particularly suitable tool to investigate the selection of these patterns are experiments conducted in thin samples using transparent organic alloys, since they allow for a direct *in situ* visualization of the interface shape by optical microscopy [3–15]. In addition to cells and dendrites, other morphologies can exist in thin samples. Examples include doublets consisting of two asymmetric fingers [5,6,8,11], disordered seaweed structures [6], and cells exhibiting regular oscillating patterns [8,13]. The orientation of the crystallographic axes of the growing solid (with respect to both the temperature gradient and the glass plates which

limit the sample) has been found experimentally to be a main factor controlling the selection of these patterns [6,13]. Thus the anisotropy of the solid-liquid interfacial energy plays a crucial role in pattern selection.

An advantage of a thin-sample geometry is that it facilitates a comparison to two-dimensional theories and numerical calculations, which are in part justified by the fact that the solutal diffusion length is typically much larger than the sample thickness. As a result, major progress has been accomplished using two-dimensional models [16–25]. The tip shape, however, remains three-dimensional even in a thin-sample geometry so that the comparison of two-dimensional models and thin-sample experiments is at best qualitative. A quantitative comparison between computations and experiments generally requires fully three-dimensional computations. Since the numerical treatment in three dimensions is considerably more difficult, only a few attempts have been made so far to tackle this problem [26–31]. One of the most exhaustive numerical studies to date by Hunt and Lu [28] was carried out using a sharp-interface model and the model predictions were compared to experiments, with good overall agreement. Limitations of this study, however, are that it was carried out for an axisymmetric shape that is independent of the azimuthal angle in a plane perpendicular to the growth direction and that it did not investigate systematically the role of the magnitude of crystalline anisotropy.

Rapid advances in phase-field modeling now make it possible to carry out efficiently and quantitatively numerical simulations of three-dimensional interfacial patterns [29–35].

Here, we use a recent model for the solidification of dilute binary alloys [36,37] to perform quantitative three-dimensional simulations of a transparent succinonitrile (SCN)-salol dilute binary-alloy system. We use this model to carry out a detailed investigation of steady-state growth shapes and tip temperatures as a function of growth rate, sample geometry, crystalline anisotropy, and also composition, and we compare some of the results to previous experimental data [15]. We carry out simulations in two dimensions and various three-dimensional geometries including thin samples of varying thickness, a regular hexagonal array of cells mimicking the pattern formation in a spatially extended three-dimensional system, and growth of an axisymmetric shape as an approximation of the growth of a cell in a regular three-dimensional hexagonal array [28].

The simulations are designed to address two long-standing issues in directional solidification. The first is the nature of the cell-to-dendrite transition. The second is the determination of the cell tip temperature. Experimentally, arrays of deep cells typically form over a finite range of velocities above v_c and dendritic arrays form for larger velocities. The transition from cells to dendrites has been observed in some experiments to be discontinuous and accompanied by a jump in primary spacing [3,4,15]. This jump in spacing appears to result from a first-order hysteretic transition with different steady-state branches of solutions for cells and dendrites, as found numerically by Hunt and Lu [28]. In other experiments, however, which exploited the ability to control the primary spacing, the cell-to-dendrite transition has been observed to be continuous [9]. As the primary spacing was increased at fixed velocity, finger-shaped deep cells with blunt tips became progressively more needlelike and developed sidebranches of progressively larger amplitude [9]. These observations suggest that the cell-to-dendrite transition can be discontinuous or continuous depending on the alloy system and growth conditions. However, the condition for the occurrence of either of those scenarios is unclear.

Understanding the mechanism of this transition is important from a fundamental standpoint since morphology selection has been a central issue in studies of pattern formation in spatially extended nonequilibrium systems. It is also important from a technological viewpoint since the primary spacing is one of the key parameters that control the mechanical properties of cast products. In particular, the tensile strength of a structural alloy is typically inversely proportional to this spacing. Cells and dendrites also produce very different microsegregation patterns (i.e., spatial distributions of solute atoms in the solidified material) that can influence other processes, such as porosity formation driven by solidification shrinkage during the late stages of solidification or the subsequent precipitation of new phases in the solid state.

To address this issue, we investigate here in detail the underlying branches of steady-state growth solutions corresponding to cellular and dendritic arrays. It is useful at this point to comment on the distinction between cells and dendrites. A simple criterion that is often used to distinguish between these two types of structures is that cells have smooth shapes while dendrites have sidebranches. For unconstrained dendrite growth along crystal axes (equiaxed growth), it is by now widely accepted that sidebranches arise

as a consequence of the amplification of thermal fluctuations [38–41]. In the case where the cell-to-dendrite transition is discontinuous, however, the existence of different branches of steady-state growth solutions for the two types of structures makes it in principle possible to distinguish between them without reference to sidebranches. In the case where the transition is continuous, as in Ref. [9], the distinction is essentially arbitrary for intermediary spacings since the interface shape evolves continuously from cell-like to needle-like and the amplitude of sidebranches also increases continuously.

In the present study, we focus on understanding the cell-to-dendrite transition from the standpoint of the underlying structure of time-independent steady-state growth solutions without thermal noise. The role of noise in sidebranching during directional solidification will be addressed in a separate paper [42]. Therefore to avoid confusion and for brevity, we refer hereafter in this paper to deep cells with blunt tips as “fingers” and to dendrites with parabolic tips, albeit no sidebranches in our present noiseless simulations, as “needles.” This choice of terminology is rooted in the analysis of two opposite limits of the steady-state growth problem, which provides the context to interpret our results. In the limit where the primary spacing is much smaller than the solutal diffusion length, neighboring cells strongly interact via the diffusion field. In this limit, the problem of directional solidification is closely related to the Saffman-Taylor (ST) viscous fingering problem [43]. From this analogy, the cell tip radius in this limit is expected to scale with the primary spacing. In the opposite limit, where the spacing is much larger than the diffusion length, cells grow essentially as isolated dendrites with a constant tip radius determined by the local supersaturation and independent of primary spacing. Whereas these two limiting cases have been recognized and analyzed by several authors [17,19,21], the precise range of validity of these analogies and the nature of the crossover between the two regimes have remained largely open.

Our results show that fingers and needles can belong to different branches of steady-state growth solutions, as one would expect for a discontinuous cell-to-dendrite transition, or belong to the same branch of solutions with a continuous shape evolution from finger to needle with increasing spacing along that branch. Distinct branches are found over a finite range of growth rates above v_c , whereas a continuous branch is found for larger velocities. Importantly, the range of velocity where discontinuous branches exist depends sensitively on the magnitude of crystalline anisotropy in all growth geometries.

At a qualitative level, this finding is a natural consequence of the fact that the tip radius of needles depends sensitively on crystalline anisotropy, as understood from microscopic solvability theory (for a review, see [44]), whereas the shape of fingers is less dependent on anisotropy. At a quantitative level, however, the branches of finger and needle growth solutions merge into a single branch over a range of primary spacing where neither of the two limits (ST and free dendrite) are exact. Thus the details of the steady-state branch solutions are not described analytically by either limit and, to our knowledge, can only be accurately described in three dimensions by the type of phase-field computations carried

out here. Those simulations allow us to pinpoint more precisely inherent limitations of the ST analogy by characterizing the dependence of the maximum finger spacing with growth rate.

The determination of the tip temperature has also been a problem of central interest in directional solidification. This temperature fixes the solute concentration in the tip region of the growing crystal and hence the final microsegregation pattern in the solid, which influences material properties. The model developed by Bower, Brody, and Flemings (BBF) [45] has been widely used in the metallurgical literature to interpret experimental data. This model predicts that the tip undercooling is determined by the growth rate and temperature gradient but is independent of cell shape. The dependence on cell shape has later been incorporated in a model developed by Karma and Pelcé (KP) [17] by exploiting the mathematical analogy between directional solidification cells and ST fingers. The latter model predicts a larger cell tip undercooling than BBF, where the undercooling is defined as the difference between the liquidus temperature and the tip temperature. The larger undercooling essentially accounts for solute rejection by a growing finger of width smaller than the primary spacing. Both the BBF and KP models are generally assumed to predict the tip temperature of cells with primary spacing smaller than the diffusion length.

Distinguishing experimentally the predictions of those models is made difficult by the inherent error in tip temperature measurements, which are typically carried out using a thermocouple or by measuring the cell tip position along the temperature gradient with respect to a known reference temperature. As a result, which model more accurately describes the cell tip temperature in an experiment has remained somewhat uncertain despite some serious attempts to settle this issue experimentally [12]. Since the present phase-field computations give a very accurate prediction of the tip temperature, they are ideally suited to test the predictions of different models. Here we find that the KP model gives a more accurate prediction of the tip temperature, as expected from the incorporation of solute rejection from a finite-width finger.

Since three-dimensional phase-field simulations are computer intensive, the choice of which simulations to carry out to gain maximum insight became important. Based on the finding that various three-dimensional geometries yield strikingly similar steady-state growth shapes and tip undercoolings, we used mainly axisymmetric simulations to perform a systematic study of the transition between fingerlike and needlelike shapes as a function of growth rate and primary spacing. As a result, for clarity of exposition, we shall present first our results for axisymmetric shapes to provide an overall picture of our main findings. We then present results for fully three-dimensional shapes in thin-sample and hexagonal-array geometries that more accurately describe experiments.

The remainder of the paper is organized as follows. In Sec. II, we review the sharp-interface and phase-field models and describe our numerical procedures. Our results are then presented and discussed in Sec. III and conclusions are presented in Sec. IV.

II. METHODS

A. Sharp-interface model

We consider a dilute binary alloy composed of a pure material (A) containing impurities (B), characterized by an idealized phase diagram with straight liquidus and solidus lines of slopes m and m/k , respectively, where k is the partition coefficient. The molar concentrations of impurities on the solid and liquid sides of the interface, c_s and c_l , satisfy the partition relation

$$c_s = kc_l. \quad (1)$$

We use the standard frozen temperature approximation, in which the temperature field is given by the externally imposed thermal gradient, whereas the release of latent heat during solidification is neglected. For a sample pulled along the z axis with a speed v_p and a thermal gradient of magnitude G directed along the same axis, the temperature field $T(z, t)$ is given by

$$T(z, t) = T_s + G(z - v_p t), \quad (2)$$

where T_s is the solidus temperature corresponding to the nominal sample composition c_0 . Furthermore, we neglect convection in the liquid, such that solute transport is entirely governed by diffusion. Since, typically, the diffusion of impurities in the liquid is several orders of magnitude larger than in the solid, we neglect the latter (one-sided model). The condition of mass conservation at the interface then yields a Stefan boundary condition

$$c_l(1 - k)v_n = -D\partial_n c|_l, \quad (3)$$

where D is the diffusion coefficient in the liquid, ∂_n denotes the derivative normal to the interface, and the subscript l indicates that the derivative is taken at the liquid side of the interface.

We assume that the solid-liquid interface is in local thermodynamic equilibrium, as appropriate for atomically rough interfaces and low growth rates. The interface temperature is then given by the Gibbs-Thomson relation, which includes the capillary shift induced by the surface tension. We consider cubic materials and use the standard expression for the surface tension

$$\gamma(\hat{n}) = \bar{\gamma}a(\hat{n}), \quad (4)$$

$$a(\hat{n}) = (1 - 3\epsilon) \left[1 + \frac{4\epsilon}{1 - 3\epsilon} (n_x^4 + n_y^4 + n_z^4) \right], \quad (5)$$

where $\bar{\gamma}$ is the average surface tension in a $\langle 100 \rangle$ plane, \hat{n} is the unit normal vector to the interface pointing into the liquid, $a(\hat{n})$ is the anisotropy function, ϵ is the strength of the fourfold anisotropy, and the coordinate system is aligned with the crystallographic axes. In two dimensions, this anisotropy function reduces to $a(\theta) = 1 + \epsilon \cos(4\theta)$, where θ is the angle between the normal direction to the interface and some underlying crystalline axis (e.g., $\langle 100 \rangle$ in a cubic crystal). With these notations, the interface temperature is given by

$$T = T_m - |m|c_l - \Gamma \sum_{i=1,2} \frac{a(\hat{n}) + \partial_{ii}a(\hat{n})}{R_i}, \quad (6)$$

where T_m is the melting temperature of the pure material, $\Gamma = \bar{\gamma}T_m/L$ is the Gibbs-Thomson coefficient with L being the latent heat of fusion per unit volume, the R_i are the principal radii of curvature of the interface, and ∂_{ii} the second derivatives along the associated principal directions.

In an alloy of nominal composition c_0 , the concentration on the liquid side of a steady-state planar interface is $c_l^0 = c_0/k$; we choose this as reference concentration. Eliminating the temperature between Eqs. (2) and (6), we obtain the standard free boundary problem for the one-sided model of directional solidification

$$\partial_t c = D\nabla^2 c, \quad (7)$$

$$c_l(1-k)v_n = -D\partial_n c|_l, \quad (8)$$

$$c_l/c_l^0 = 1 - (1-k)d_0 \sum_{i=1,2} \frac{a(\hat{n}) + \partial_{ii}a(\hat{n})}{R_i} - (1-k)(z - v_p t)/l_T, \quad (9)$$

where the capillarity length d_0 is given by

$$d_0 = \frac{\Gamma}{\Delta T_0} = \frac{\bar{\gamma}T_m}{L|m|(1-k)c_l^0}, \quad (10)$$

with $\Delta T_0 = |m|(1-k)c_l^0$ being the freezing range and the thermal length l_T is defined as

$$l_T = \frac{\Delta T_0}{G} = \frac{|m|(1-k)c_l^0}{G}. \quad (11)$$

The characteristic length scales of the problem are then d_0 , l_T , and the diffusion length

$$l_D = \frac{D}{v_p}. \quad (12)$$

The multiscale character of the problem originates from the fact that, for slow solidification, d_0 is several orders of magnitude smaller than the other two length scales.

In the axisymmetric approximation, we define the azimuthally averaged anisotropy function

$$\bar{a}(\theta) = \int_0^{2\pi} \frac{d\phi}{2\pi} a(\theta, \phi), \quad (13)$$

where θ is the angle between the normal to the solid-liquid interface and the growth axis and ϕ is the azimuthal angle in the plane perpendicular to the growth direction. Using Eq. (5) with $a(\hat{n})$ expressed in terms of θ and ϕ , we find

$$\bar{a}(\theta) = (1-3\epsilon) \left[1 + \frac{4\epsilon}{1-3\epsilon} \left(\cos^4 \theta + \frac{3}{4} \sin^4 \theta \right) \right]. \quad (14)$$

Furthermore, for an axisymmetric shape independent of ϕ , the interface condition becomes [46]

$$c_l/c_l^0 = 1 - (1-k)d_0 \left[\frac{A(\theta)}{R_1} + \frac{B(\theta)}{R_2} \right] - (1-k)(z - v_p t)/l_T,$$

where $A(\theta)$ and $B(\theta)$ are defined by

$$A(\theta) = \bar{a}(\theta) + \frac{d^2 \bar{a}(\theta)}{d\theta^2}, \quad (15)$$

$$B(\theta) = \bar{a}(\theta) + \cot \theta \frac{d\bar{a}(\theta)}{d\theta}. \quad (16)$$

In addition, the radii of curvatures are given by

$$\frac{1}{R_1} = -\frac{d}{dr} \left[\frac{z'}{(1+z'^2)^{1/2}} \right], \quad (17)$$

$$\frac{1}{R_2} = -\frac{z'}{r(1+z'^2)^{1/2}}. \quad (18)$$

Here, $z(r)$ parametrizes the axisymmetric growth shape in cylindrical coordinates (r, θ) , where r is the radial coordinate of the interface in a plane perpendicular to the growth axis and $z' \equiv dz(r)/dr$.

B. Phase-field model

The phase-field method has the well-known advantage to avoid front tracking and has been extensively developed to simulate solidification morphologies (for a review, see [47]). Here we use a phase-field formulation designed to carry out quantitative simulations of alloy solidification on experimentally relevant length and time scales in the slow growth rate limit where the solid-liquid interface can be assumed to be in local thermodynamic equilibrium [36,37]. To be computationally tractable, such simulations generally require choosing the width W of the spatially diffuse interface in the phase-field model about one order of magnitude smaller than the characteristic scale of the solidification pattern and thus much larger than the real nanometer width of the solid-liquid interface. This thick interface generates an anomalously large solute trapping effect, which is canceled by the introduction of a phenomenological ‘‘antitrapping current’’ [36,37]. The quantitative accuracy of this method has been demonstrated for both the isothermal [36] and the directional [37] solidification of a dilute binary alloy. Since the equations for directional solidification have been presented and discussed in detail in Ref. [37], we will comment here only on some points that are specific to the simulations of the present paper.

C. Numerical implementation

For the full three-dimensional simulations, the equations of motion of the phase-field model [Eqs. (68) and (69) of Ref. [37]] are discretized on a simple-cubic lattice. For the axisymmetric approximation, the interface boundary condition is handled automatically by solving the equations in cylindrical coordinates with the azimuthally averaged surface energy anisotropy given by Eq. (14) that only depends on θ , as described in the Appendix. The grid spacing for the

TABLE I. Material parameters of the SCN-salol system.

Liquidus slope	m (K/wt %)	-0.68
Partition coefficient	k	0.1
Impurity diffusivity (liquid)	D ($\mu\text{m}^2/\text{s}$)	800
Gibbs-Thomson constant	Γ (K μm)	0.0644
Surface tension anisotropy	ϵ	0.007

finite difference discretization is fixed to $\Delta x = \Delta y = \Delta z = 0.8W$ on the cubic lattice and $\Delta r = \Delta z = 0.8W$ in cylindrical coordinates. In order to minimize the anisotropy created by the grid, a maximally isotropic discretization of the Laplace operator involving first- and second-neighbor grid points is used. It was shown in Ref. [37] that this offers a good compromise between accuracy and computational efficiency. The equations are integrated in time using an explicit Euler scheme.

Since, away from the interface, the concentration field obeys the diffusion equation and the phase field is constant, we use a simple adaptive meshing algorithm that coarsens the mesh ahead of the interface, as briefly described in Ref. [48]. As a result, most of the computation time is spent solving the phase-field equations in the region occupied by the cellular array structure, whereas the long-range diffusion field that extends ahead of this structure is treated with minimal computational effort. This makes it possible to simulate three-dimensional samples for experimental growth conditions.

Simulations start from a single seed of solid that is placed in the corner of the simulation box. It rapidly develops into a cellular shape. The simulation box is periodically shifted and the rear cut off in order to reduce simulation time; the box is large enough to contain a portion of solid that is about two cell spacings long. At the rear end of the box, we apply no-flux boundary conditions for both the phase field and the concentration field. Thus, we omit the dynamics of the grooves as well as the flux of solute that comes from the root of the grooves. We have checked by performing simulations with varying cutoff length that this procedure does not significantly alter the tip shape or the tip undercooling.

The values for the relevant materials parameters for the SCN-salol system are listed in Table I. Unless specified otherwise, the nominal sample concentration is $c_0 = 0.7$ wt % salol. The surface-tension anisotropy is the one estimated for pure succinonitrile. To explore the role of anisotropy, we also performed simulations with different anisotropy strengths while keeping the other parameters unchanged.

An important point is the choice of the interface thickness W introduced in the phase-field model. The precision of the results increases when W decreases, but so does the computation time. It was shown in Ref. [37] that the outcome of the simulations does not appreciably depend on W as long as it remains about one order of magnitude smaller than any relevant length scale of the problem. Usually, the smallest scale to be taken into account is the tip radius. This implies that W can be chosen much larger than the capillary length d_0 . We have used the value $W/d_0 = 82$ ($W \approx 1.25 \mu\text{m}$), which provides simulations that are converged to within a few percent

of the sharp-interface limit, both for the tip radius and the tip undercooling. Different cell spacings were simulated by keeping the interface thickness W fixed and by varying the size of the simulation box.

The two most important quantities characterizing the geometry of a cell are the tip radius and the position of the tip with respect to the isotherms (which is equivalent to the tip temperature). For the axisymmetric approximation, the tip radius is unique, whereas a three-dimensional cell has two radii of curvature which are in general distinct. Here, we focus on the in-plane radius of curvature ρ (measured on a cut along the sample plane), since it is the only one that can be determined with a good precision in experiments. To characterize the tip position, we use the dimensionless tip undercooling Δ given by

$$\Delta = \frac{T_l - T_{\text{tip}}}{T_l - T_s} = \frac{T_l - T_{\text{tip}}}{|m|(1-k)c_l^0} = 1 - \frac{z_{\text{tip}}}{l_T}, \quad (19)$$

where T_{tip} is the tip temperature, T_l and T_s are the liquidus and solidus temperatures for the composition c_0 , respectively, and z_{tip} is the tip position with respect to the isotherm of the solidus temperature T_s . Since $T_s \leq T_{\text{tip}} \leq T_l$, we have $0 \leq \Delta \leq 1$.

III. RESULTS AND DISCUSSION

A. Steady-state branches of finger and needle growth solutions

Let us start by discussing the results of axisymmetric simulations. These simulations describe accurately the growth of a single cell in a cylindrical tube. They are also a good approximation for cells in an extended hexagonal array. Indeed, for perfectly periodic hexagonal states, planes of symmetry run along the grooves surrounding a cell. Therefore, the steady-state solution for the full array can be obtained by solving the problem for a single cell inside a hexagonal prism with reflection boundary conditions on the sides, which is quite well approximated by the solution inside a cylinder. Since axisymmetric simulations are effectively two-dimensional, they are much faster than the full three-dimensional computations and allowed us to explore efficiently a larger range of parameters.

We found two distinguishable types of cell shapes illustrated in Fig. 1. For small spacings, cells have a blunt tip, whereas for large spacings, the tip becomes sharper and acquires a parabolic shape. As mentioned in Sec. I, we refer to these two types of steady-state growth solutions as fingers and needles, respectively. We found that the existence of these two types of solutions and the nature of the transition between them, whether discontinuous or continuous, are influenced by two main factors: the pulling speed and the crystalline anisotropy. When the transition is discontinuous, fingers and needles belong to different branches of steady-state growth solutions. When it is continuous, fingers evolve progressively into needles with increasing spacing at fixed growth rate and the distinction between fingers and needles becomes blurred for intermediate spacings.

The influence of the pulling speed can best be visualized by fixing the anisotropy and plotting the available steady-

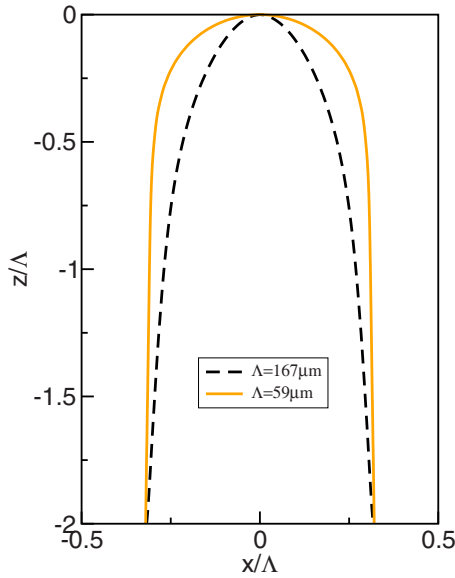


FIG. 1. (Color online) Examples of steady-state cell shapes with blunt and parabolic tips referred to for brevity in this article as fingers (continuous line) and needles (dashed line), respectively. Parameters are $G=38$ K/cm, $v_p=5.0$ $\mu\text{m/s}$, $c_0=0.7$ wt %, and $\epsilon=0.015$. The cell spacing is $\Lambda=59$ μm for the finger and $\Lambda=167$ μm for the needle.

state spacings for different pulling speeds, as shown in Fig. 2. Three regimes can be distinguished, separated by vertical dashed lines. In the low-velocity regime (I) only fingers (F) form and no needles exist. In the intermediate-velocity regime (II), fingers and needles coexist ($F\&N$) on separate branches of steady-state growth solutions for small and large spacings, respectively, separated by a “gap” in which no

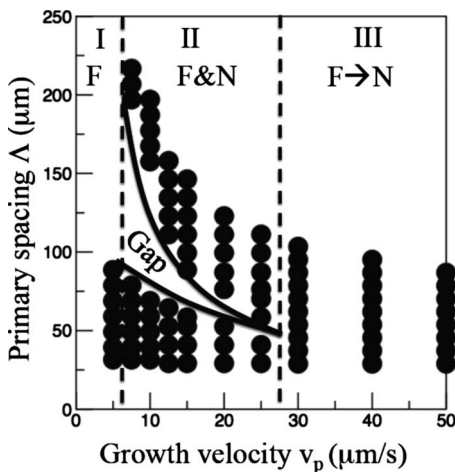


FIG. 2. Range of spacings for the existence of finger (F) and needle (N) axisymmetric steady-state growth solutions as a function of growth velocity v_p for $G=38$ K/cm, $c_0=0.7$ wt %, and $\epsilon=0.01$. Three different growth regimes can be distinguished with only fingers (F) for low velocity (regime I), distinct branches of finger and needle solutions ($F\&N$) for intermediate velocities (regime II), and merging of these branches into a single branch with a continuous shape evolution from finger to needle ($F\rightarrow N$) with increasing spacing (regime III).

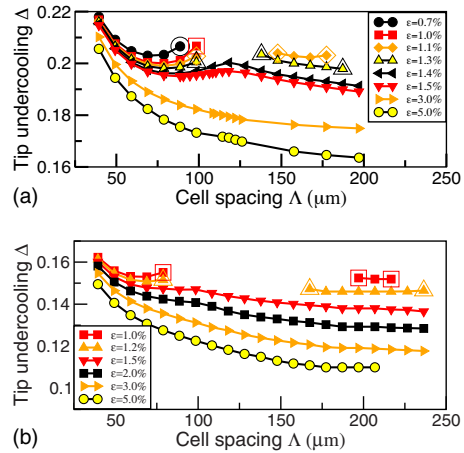


FIG. 3. (Color online) Dimensionless tip undercooling Δ of axisymmetric finger and needle steady-state growth shapes vs cell spacing for different anisotropy strengths. The parameters are $G=38$ K/cm, $c_0=0.7$ wt %, and $v_p=5.0$ $\mu\text{m/s}$ in (a) and $v_p=7.5$ $\mu\text{m/s}$ in (b). The limits of stability of finger and needle branches are marked by a larger empty symbol surrounding a filled symbol. The results show that increasing anisotropy strength extends the limits of existence of needles to lower growth rate.

steady-state growth was found. Finally, in the high-velocity regime (III), the two separate branches merge into a single one, along which the shape changes continuously from fingerlike to needlelike ($F\rightarrow N$) with increasing spacing.

The existence of these three distinct growth regimes is in reasonably good quantitative agreement with thin-sample directional solidification experiments carried out for the same parameters ($G=38$ K/cm and $c_0=0.7$ wt % salol) and different pulling velocities [15]. The sample thickness in those experiments was comparable to the primary spacing. The results can be meaningfully interpreted in the context of the branch structure of Fig. 2 for axisymmetric steady-state growth shapes because this structure turns out to be weakly dependent on growth geometry as discussed further below. The experimental results identified three growth regimes with only cells for $v_p < 8$ $\mu\text{m/s}$, coexistence of cells and dendrites for 8 $\mu\text{m/s} < v_p < 20$ $\mu\text{m/s}$, and only dendrites for $v_p > 20$ $\mu\text{m/s}$. Furthermore, dendritic arrays were observed to grow with a larger spacing than cellular arrays over the intermediate-velocity range where both structures coexist. Even though the hysteretic character of the transition was not investigated explicitly in those experiments, the branch structure of Fig. 2 supports a scenario where the array spacing makes discontinuous upward and downward jumps when the growth velocity is cycled (i.e., increased and decreased in small steps) over a range that crosses the boundary between the low-velocity regime (I) where only cells exist and the intermediate regime (II) where both cells and dendrites coexist. Note that this hysteresis cycle depends both on the existence of a spacing gap in regime II and on the absence of steady-state needle solutions below a critical velocity.

Curves of tip undercooling versus spacing for various values of the anisotropy are shown in Fig. 3 for $v_p=5$ $\mu\text{m/s}$ and $v_p=7.5$ $\mu\text{m/s}$. These diagrams can be best understood when considering the curves in the order of de-

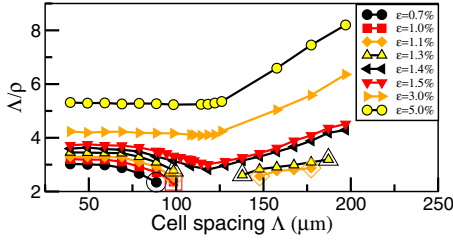


FIG. 4. (Color online) Ratio of cell spacing Δ and tip radius ρ of axisymmetric growth shapes for $G=38$ K/cm, $c_0=0.7$ wt %, $v_p=5.0$ $\mu\text{m/s}$, and different anisotropy strengths. This ratio is constant for finger shapes that scale with the cell spacing and increases linearly with Δ for needles that have a constant ρ at fixed v_p .

creasing anisotropy. For strong anisotropy, a continuous branch of solutions extends from small to large spacings and the tip undercooling decreases with increasing spacing (regime III). When the anisotropy is lowered, the curve of tip undercooling versus spacing becomes nonmonotonous and exhibits a maximum for intermediate cell spacings. The transition from fingerlike to needlelike shapes occurs over a narrow spacing range close to this maximum. For even lower anisotropy, a “gap” opens, but both finger and needle solutions still exist (regime II). Finally, below a critical anisotropy strength, the needle branch ceases to exist and only the cell solution subsists (regime I). When a gap exists, a tip-splitting instability occurs at the upper end of the finger branch and on both ends of the needle branch; on the latter, it is sometimes preceded by oscillations. These limits are marked in Fig. 3 by larger empty symbols surrounding filled symbols. When there is no such symbol at the end of a curve, we just stopped following the branch of steady-state growth solutions for computational cost saving.

The combined results of Figs. 2 and 3 clearly show that the transitions between the different regimes I, II, and III depend both on growth velocity and anisotropy strength, with the regimes II and III including needles extending to lower velocity with increasing anisotropy strength.

In Fig. 4, we show the ratio of cell spacing Δ and tip radius ρ for the same set of calculations as Fig. 3(a). For low spacings, this ratio is constant for all anisotropies, which means that the tip radius scales with the cell spacing. In contrast, for high spacings, Δ/ρ is approximately proportional to Δ , which simply means that the tip radius is constant. These are indeed the behaviors expected for strongly and weakly interacting cells, respectively. For high anisotropies, the transition between these two regimes is surprisingly sharp. When regime II (the opening of the gap) is approached, the crossover becomes more extended and in regimes I and II, the scaling of ρ with Δ on the finger branch is lost when the gap is approached. Note, however, that the typical cell spacing at which the crossover occurs is independent of the anisotropy strength. This is consistent with the hypothesis that this crossover is governed by the ratio of cell spacing and solutal diffusion length.

B. Tip undercooling

Next, let us discuss the comparison of our simulation data to the available theories for the tip undercooling. Figure 5

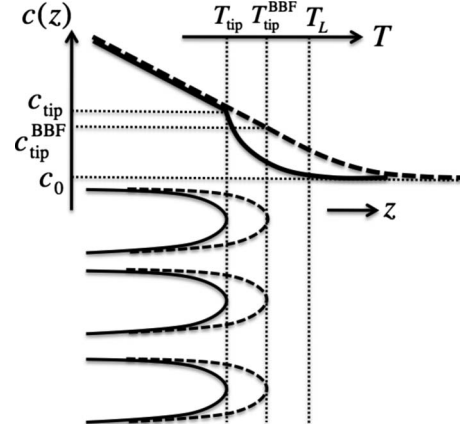


FIG. 5. Schematic representation of cellular fronts and corresponding tip temperatures and concentration profiles along the growth direction for the BBF model (dashed lines) and Karma-Pelcé model (solid lines).

shows a schematic representation of cellular fronts that highlights the relationship of the tip position and undercooling to the form of the concentration profiles assumed in the BBF and KP models. In both the BBF and KP models, the solute concentration on the liquid side of the interface is assumed to follow the liquidus and hence to vary linearly with z in the presence of a linear temperature gradient. Furthermore, in both models, the concentration field ahead of the solidification front is taken to have the simple exponential form

$$c(z) = (c_{\text{tip}} - c_0)\exp(-v_p z/D) + c_0, \tag{20}$$

which neglects the lateral (x) variation of the concentration field on the scale of the solutal diffusion length D/v_p . In the BBF model, the impurity flux determined by Eq. (20) at the tip position, $v_p(c_{\text{tip}} - c_0)$, is assumed to balance the flux $-G/m$ induced by the linear variation of concentration along the interface. Using the fact that $m(c_{\text{tip}} - c_0) = T_{\text{tip}} - T_l$, where T_l is the liquidus temperature, this flux balance condition yields the well-known BBF relation $T_{\text{tip}} = T_L - GD/v_p$, or

$$\Delta_{\text{BBF}} = \frac{D}{v_p l_T}, \tag{21}$$

in terms of the dimensionless tip undercooling used in this paper. This flux balance also implies that the slope of the concentration profile in the BBF model is continuous when traversing the tip region, as illustrated by the thick dashed line in Fig. 5. The KP model differs from the BBF model in that it also takes into account the impurity flux generated by the moving interface through the modified tip flux balance condition [17]

$$-D \frac{dc}{dz} = f_s c_0 (1 - k) v_p - (1 - f_s) D \frac{G}{m}, \tag{22}$$

where f_s is the solid fraction in a region behind the tip where the finger width can be assumed constant. This expression yields the prediction for the tip undercooling

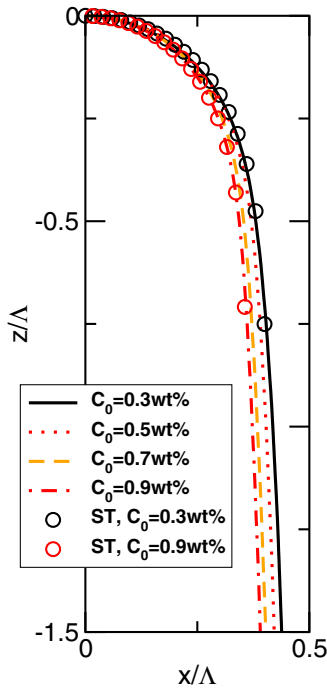


FIG. 6. (Color online) Axisymmetric growth shapes for different concentrations of salol for $v_p=5.0 \mu\text{m/s}$, $G=38 \text{ K/cm}$, and $\epsilon=0.007$. For each concentration, the shape shown corresponds to the finger solution with the largest spacing. The spacings are given in Fig. 8 below.

$$\Delta_{\text{KP}} = \frac{f_s k + (1 - f_s) \frac{D}{v_p l_T}}{1 - f_s(1 - k)}, \quad (23)$$

which reduces to the BBF expression in the limit where f_s vanishes. For finite f_s , however, it predicts a larger undercooling ($\Delta_{\text{KP}} > \Delta_{\text{BBF}}$) that is necessary to accommodate the solute rejection of the moving tip as illustrated in Fig. 5 where the concentration profile (thick solid line) has a discontinuous slope at the tip. Furthermore, this undercooling approaches unity in the limit $f_s=1$ corresponding to planar interface growth.

Equation (23) generally needs to be supplemented by an expression for f_s to predict the tip undercooling. In two dimensions (2D), KP exploited the mathematical analogy between directional solidification and the ST viscous fingering problem [43] to obtain an expression for f_s that is simply equal in this case to the relative finger width λ , defined as the ratio of the cell width to the primary spacing. In three dimensions (3D), the same analogy holds in the limit $\Lambda v_p/D \ll 1$. Even though there is no known analytical solution in 3D, the form

$$\frac{z}{\Lambda} = \frac{\lambda^2 \Lambda}{\pi^2 \rho} \log\left(\cos \frac{\pi r}{\lambda \Lambda}\right) \quad (24)$$

was found by Levine and Tu [49] to provide a good fit to numerically computed axisymmetric ST shapes with relative finger width λ (defined as the ratio of the cell width to the tube diameter). This form also fits well here the tip region of

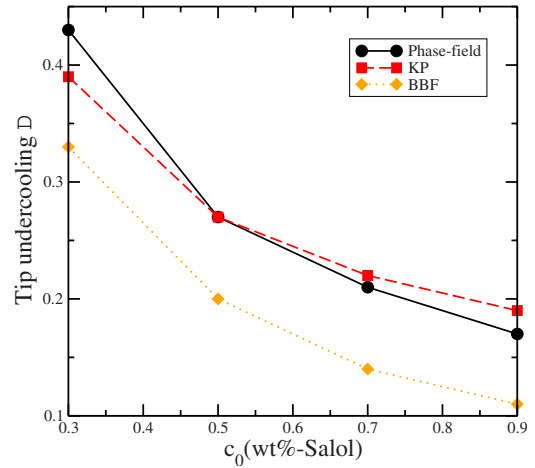


FIG. 7. (Color online) Variation of dimensionless cell tip undercooling with salol concentration computed from phase-field simulations and predicted by the BBF and KP models for $v_p=5.0 \mu\text{m/s}$, $G=38 \text{ K/cm}$, and $\epsilon=0.007$. The values of λ that are needed for the KP prediction are obtained from fits of the cell tip to the Saffman-Taylor shape.

axisymmetric solidification fingers, as found previously [50] and illustrated in Fig. 6, and those fits were used to compute $f_s=\lambda^2$ for different finger shapes. To test the BBF and KP theories, we fixed v_p and G and extracted finger shapes and tip undercoolings from phase-field simulations for different spacings Λ . We studied several compositions in order to vary the freezing range. The theoretical predictions for the tip undercooling are compared to the phase-field results in Fig. 7. For each composition, the undercooling displayed in the figure corresponds to the largest stable spacing of the finger branch (the corresponding spacings are given in Fig. 8 below). Since, for fixed composition, v_p , and G the tip undercooling is only weakly dependent on primary spacing, the undercooling corresponding to the maximum spacing of the finger branch is representative of other spacings. It can be clearly seen that the KP prediction is much closer to the simulation data than the BBF model.

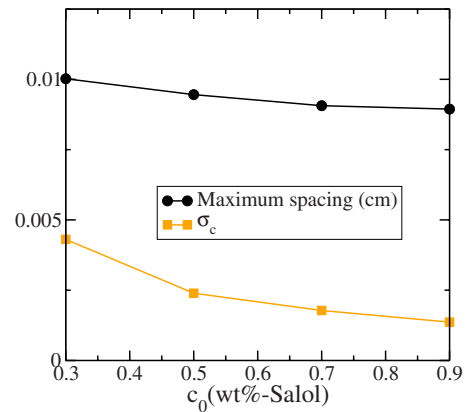


FIG. 8. (Color online) Variation of maximum finger spacing and critical value of the dimensionless surface-tension parameter at this spacing, σ_c , with concentration for $v_p=5.0 \mu\text{m/s}$, $G=38 \text{ K/cm}$, and $\epsilon=0.007$.

C. Maximum finger spacing

The steady-state branch of fingers terminates at a maximum spacing for velocities smaller than the velocity at which the finger and needle branches merge to form a single continuous branch (regimes I and II in Fig. 2). Levine and Tu [49] found numerically that steady-state axisymmetric ST finger solutions only exist above a minimum value of a dimensionless surface-tension parameter. When mapping directional solidification to the ST problem in the limit $v_p \Lambda / D \ll 1$, this surface-tension parameter can be defined as

$$\sigma = \frac{d_0 D}{\Lambda^2 v_p} \left[\frac{1 - f_s(1 - k)}{k + [f_s(1 - k) - 1] \frac{D}{v_p l_T}} \right]. \quad (25)$$

Thus, for fixed control parameters G and v_p , the existence of a minimum value of σ , defined here by σ_c , would imply the existence of a maximum solidification finger spacing Λ_{max} , implicitly defined by

$$\sigma_c = \frac{d_0 D}{\Lambda_{max}^2 v_p} \left[\frac{1 - f_s(1 - k)}{k + [f_s(1 - k) - 1] \frac{D}{v_p l_T}} \right], \quad (26)$$

if the analogy between ST and solidification fingers holds. To test validity of this analogy, we plot together in Fig. 8 the maximum cell spacing Λ_{max} and σ_c values computed with Eq. (26) for fixed v_p and G and the same compositions as in Fig. 7. The maximum spacing is found to only vary by about 10% over this wide range of compositions while σ_c decreases by a factor of roughly 3. This decrease is mainly due to the fact that the chemical capillary length d_0 defined by Eq. (10) is inversely proportional to the alloy composition c_0 , which itself varies by a factor of 3 in this plot. The variations of σ_c due to the dependence of f_s and l_T on the composition are much smaller. If the analogy between ST and solidification fingers were to be valid [Eq. (26) were to hold], Λ_{max} should decrease by a factor of $1/\sqrt{3}$ over this range of composition because d_0 decreases by a factor of 3 and σ_c is constant in this analogy. The fact that, instead, Λ_{max} decreases by only 10% and σ_c decreases by a factor of 3 in Fig. 8 shows unequivocally that the maximum spacing is not predicted by the analogy between solidification and ST fingers. We note that the minimum value σ_c for the existence of ST fingers found by Levine and Tu was determined for an isotropic surface tension, whereas the present simulations include anisotropy. However, since the maximum finger spacing does not depend sensitively on anisotropy strength for small anisotropy in our simulations (Fig. 3), inclusion of a weak anisotropy in the ST problem is not likely to resolve this discrepancy.

More insights concerning the maximum finger spacing can be gained by considering its dependence on the pulling speed. In Fig. 9, we plot the square of the maximum finger spacings found in the simulations of Fig. 2 versus the inverse of the pulling speed, $1/v_p$. The result is well fitted by a straight line going through the origin (dashed line). This means that $\Lambda^2 v_p$ is roughly constant. Even though the tip radius is not strictly proportional to Λ close to the maximum

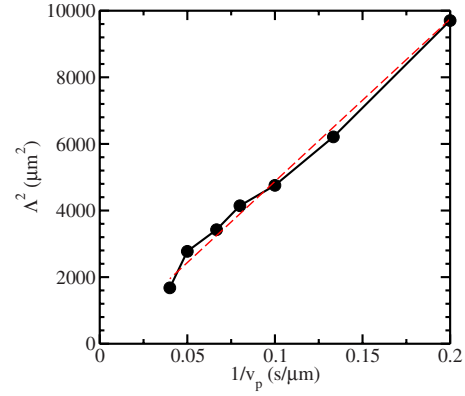


FIG. 9. (Color online) Square of the maximum finger spacing vs inverse pulling speed, $1/v_p$, for the same data shown in Fig. 2 ($G = 38$ K/cm, $\epsilon = 0.01$). It is well fitted by a straight line going through the origin (dashed line).

finger spacing, one can still infer from this finding that $\rho^2 v_p$ is roughly constant. We are thus faced with the somewhat surprising conclusion that, whereas the shapes of the fingers are well fitted by the ST form, the $1/\sqrt{v_p}$ dependence of the maximum finger spacing on growth rate is characteristic of dendrites.

A possible interpretation of these findings can be obtained by a finer analysis of the ST analogy, taking into account results on another related and well-known problem, namely, the growth of a crystalline finger in a channel [51,52]. Formally, the only difference between these two problems is that the Laplace equation of the ST problem is replaced by the diffusion equation for crystal growth. One might naively expect that for slow growth, the diffusion equation tends to the Laplace equation and that the two problems are perfectly equivalent. However, previous analyses [51,52] show that while there is indeed a branch of solutions for the crystal-growth problem that maps onto the ST solutions, there is a second, “diffusive” branch of solutions, which always grows faster than the ST solutions. The *shape* of these fingers is still well described by the ST shape, but the relation between undercooling and growth speed is entirely different. Our findings suggest that the same is true in three dimensions: whereas the 3D ST shape found by Levine and Tu closely describes the axisymmetric solidification fingers in our simulations, which justifies the use of this shape for computing the tip undercooling using the KP theory as we have done here, those fingers belong to a faster growing branch of steady-state growth solutions that are distinct from the 3D ST branch. This plausible scenario provides a natural explanation for why the ST analogy fails to predict the maximum finger spacing.

D. Full three-dimensional simulations

Let us now turn to the results of full three-dimensional simulations. Even with a powerful model and a multiscale implementation, three-dimensional simulations of extended cellular arrays for realistic materials parameters remain computationally challenging. Therefore, we restrict our attention to perfectly periodic arrays; furthermore, we only consider

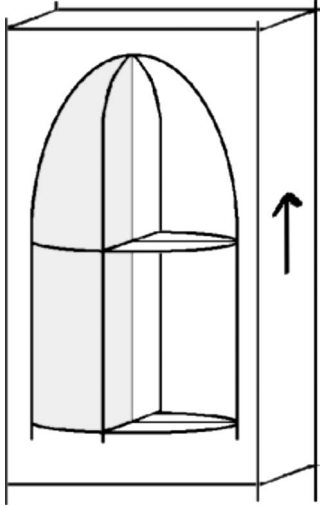


FIG. 10. Sketch of the reflection symmetry in the thin-sample geometry for cubic crystal symmetry with one crystallographic axis aligned with the temperature gradient and the arrow pointing along the growth direction.

samples in which one crystallographic axis is aligned with the temperature gradient and another one with the sample plane, such that the third one is normal to the sample walls. This makes it possible to exploit the symmetries of the pattern to reduce computation time, as illustrated in Fig. 10. In a thin sample with a single row of cells, the midplane between the two plates and the midplane between two cells are planes of mirror symmetry along the x and y directions, respectively. Therefore, simulations conducted in a box of size $\Lambda/2$ along x and $\delta/2$ along y with reflection boundary conditions on the lateral sides, and with a quarter of a cell placed in one corner, are equivalent to simulations of the full periodic array. Note that the reflection boundary condition for the phase field on the side that corresponds to the sample wall is equivalent to imposing a contact angle of 90° between the solid-liquid interface and the sample walls. Other contact angles could be easily simulated by modifying this boundary condition [30], but (i) there is at present no reliable information about the real value of this contact angle in experiments and (ii) for well-developed three-dimensional cells or dendrites, the interface comes into contact with the sample walls only far behind the tip and therefore this boundary condition has no influence on tip shape or undercooling.

For comparison, we have also performed simulations for perfectly periodic three-dimensional hexagonal arrays. As shown in Fig. 11, in this case we can take advantage of the two orthogonal mirror-symmetry planes that run across the center of each cell and the center of symmetry that is present exactly half way between two cell centers. In order to obtain a perfectly hexagonal array, the aspect ratio of the box sizes along x and y should be $\sqrt{3}/2$. On a uniform cubic grid, this irrational aspect ratio cannot be achieved exactly; we chose the closest possible rational approximation for the box size. As will become clear below, this approximation does not have any significant influence on our simulation results.

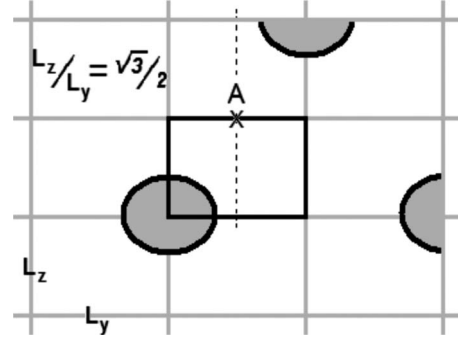


FIG. 11. Top view sketch showing the boundary conditions that create a hexagonal arrangement from a quarter of a cell (in the shadowed domain). Nonflux boundaries are imposed on all boundaries of the computational domain (thick solid lines) except the upper boundary where a point symmetry with respect to the center point A (marked with a cross) is imposed.

E. Influence of geometry

Examples of steady-state cell shapes calculated in three dimensions in hexagonal and thin-sample geometries are shown in Fig. 12. In the thin-sample geometry, when the sample thickness δ is smaller than some threshold δ_{min} (which for this set of parameters is between 22 and 33 μm), the cell shape adopts a bidimensional “ribbon” form.

In Fig. 13 we show the cell shapes, scaled with the cell spacing, for identical simulation parameters but different geometries. For the thin-sample and hexagonal geometries, the plotted shape is a cut through the center of the cell. Since the three-dimensional cell shapes are always convex, this would also correspond to the “projected shape” that can be directly observed in thin-sample experiments. The scaled cell shapes in hexagonal, thin-sample, and axisymmetric geometries are all close to each other and to the scaled shape obtained from experimental data. In contrast, they are markedly different from the ribbon state which, as expected, almost coincides with the two-dimensional solution.

Figure 14 presents the tip undercooling of steady-state cells as a function of cell spacing in the different geometries explored. The tip undercooling for bidimensional steady states is systematically larger than for the corresponding three-dimensional geometries. Among the three-dimensional geometries, there are no major discrepancies. The difference

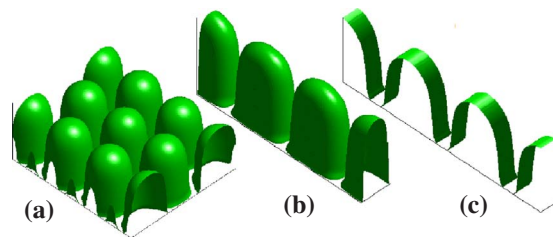


FIG. 12. (Color online) Steady-state cell shapes for $G = 38 \text{ K/cm}$, $c_0 = 0.7 \text{ wt \%}$, and $v_p = 5 \text{ }\mu\text{m/s}$ for a hexagonal array with (a) cell spacing $\Lambda = 95 \text{ }\mu\text{m}$, and in a thin-sample geometry with cell spacing $\Lambda = 95 \text{ }\mu\text{m}$, for a sample thickness of (b) $\delta = 33 \text{ }\mu\text{m}$ and a sample thickness of (c) $\delta = 22 \text{ }\mu\text{m}$.

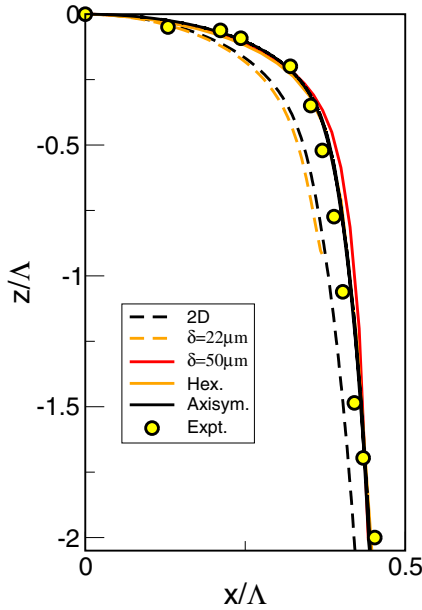


FIG. 13. (Color online) Scaled steady-state scaled cell shapes ($G=38$ K/cm, $c_0=0.7$ wt %, and $v_p=5.0$ $\mu\text{m/s}$), with cell spacing of $\Lambda=96$ μm for the bidimensional case, $\Lambda=95$ μm for the thin-sample and hexagonal geometries, and $\lambda=92$ μm for the axisymmetric case. The shape is compared to experimental data obtained from the analysis of a steady-state shape with $G=50$ K/cm, $v_p=5.0$ $\mu\text{m/s}$, and $\Lambda=106$ μm .

between the axisymmetric solution and the two genuinely three-dimensional states is larger than the one between the latter.

In agreement with a previous study [50], we found that the dimensionality strongly affects quantitatively the finger and needle branch structure: whereas all the three-dimensional geometries exhibit only finger solutions up to a maximum spacing that is almost independent of the geometry (corresponding to regime I in Fig. 2), two-dimensional solutions and ribbon states exist beyond this limit and continuously connect to the dendrite solutions (corresponding to regime III in Fig. 2). Dimensionality, however, does not affect qualitatively the branch structure. A similar branch structure with the same dependencies on pulling speed and anisotropy was found previously for bidimensional steady-states of the symmetric model of directional solidification (equal diffusivity of impurities in the solid and liquid) [53].

Concerning the nature of the cell-to-dendrite transition, the same branch structure as for the axisymmetric states is found in the thin-sample geometry, as shown in Fig. 15. Since these simulations take much longer than the axisymmetric ones, we repeated only the runs that are most critical for revealing the structure of the diagram. In particular, it can be seen that the opening of the gap and the disappearance of the dendrite branch occur at about the same anisotropies in both cases and that the values of the critical spacings limiting the gap are very similar. The most visible difference between axisymmetric and thin-sample solutions concerns the low-anisotropy limit of the needle branch: whereas needle solutions are already present for $v_p=5.6$ $\mu\text{m/s}$ and $\epsilon=1\%$ in thin samples, they appear only at slightly higher pulling

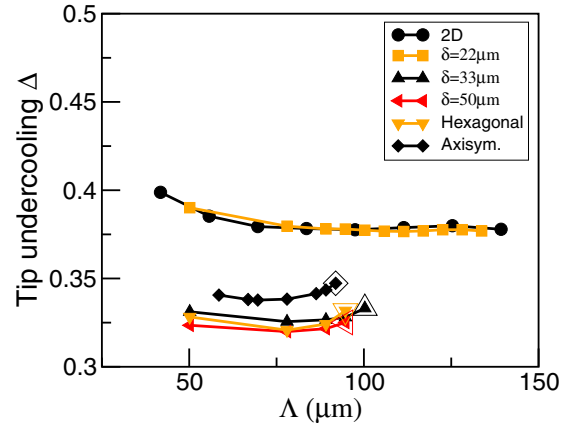


FIG. 14. (Color online) Tip undercooling of steady-state cells as a function of cell spacing in different geometries (These results are a direct comparison to Ref. [50]. Thus, for these simulations, we have used the value of the partition coefficient $k=0.16$ of Ref. [50] rather than the value $k=0.1$ of Table I used in all the other simulations. However, this does not change the qualitative aspects of our results as far as the dependence of the tip undercooling on the sample geometry is concerned.) with $G=38$ K/cm and $v_p=5.0$ $\mu\text{m/s}$. The thin-sample geometry is characterized by the cell thickness δ , and we include the case when the steady-state shape corresponds to a “ribbon” equivalent to the bidimensional case ($\delta=22$ μm). The limits beyond which we did not find steady-states are marked by a larger empty symbol surrounding a filled symbol.

speed (or anisotropy) in the axisymmetric case. It should be mentioned that both in the axisymmetric and in the thin-sample geometries, these low-anisotropy needle states were difficult to reach: simulations had to be started with a steady-state solution at higher anisotropy as an initial condition.

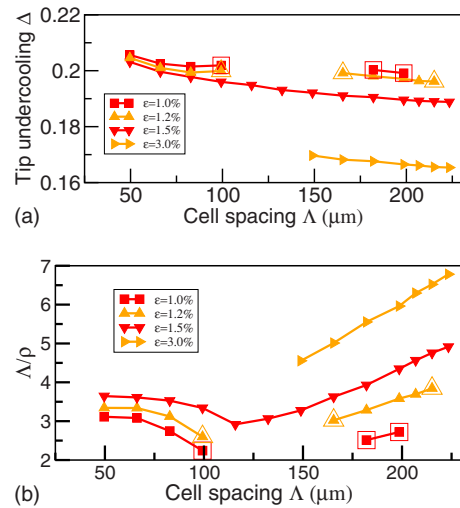


FIG. 15. (Color online) Tip undercooling and tip radius for thin-sample steady states, with thickness $\delta=50$ μm , obtained for $G=38$ K/cm, $c_0=0.7$ wt %, and a pulling speed of $v_p=5.0$ $\mu\text{m/s}$. The limits beyond which we did not find steady states are marked by a larger empty symbol surrounding a filled symbol; otherwise, we just stopped following the solution branches. In particular, finger growth shapes would of course exist for smaller spacing for $\epsilon=3\%$, but we have not calculated them here.

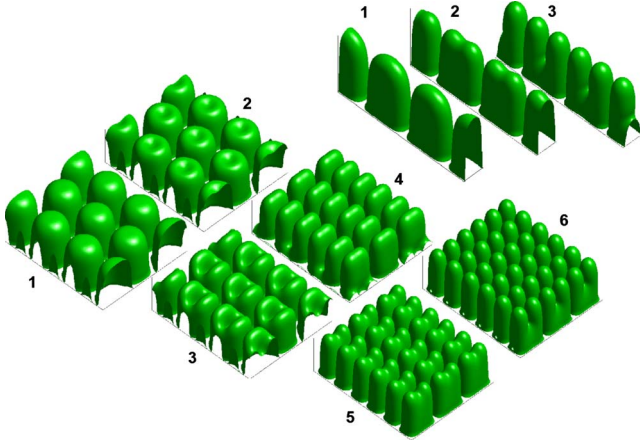


FIG. 16. (Color online) Sequence showing a tip-splitting instability in thin-sample geometry with thickness $\delta=50 \mu\text{m}$ and initial cell spacing $\Lambda=110 \mu\text{m}$ and in an initially hexagonal array with initial cell spacing $\Lambda=110 \mu\text{m}$, in both $G=38 \text{ K/cm}$ and $v_p=5.0 \mu\text{m/s}$.

F. Instabilities and symmetries

Beyond the maximum steady-state spacing on the cellular branch, a tip-splitting instability occurs, the details of which depend on the geometry, as shown in Figs. 16 and 17. As can be appreciated from the latter figure, in the hexagonal case, the tip-splitting instability can involve a change of symmetry of the pattern. In the axisymmetric geometry, the instability proceeds via the appearance of a central dip in the cell tip, which has no other choice but to stay circular. It should also be noted that, whereas the tip splitting is sometimes preceded by oscillations on the needle branch in the axisymmetric simulations, such oscillations are never found in the other geometries, where the instability is just a standard (steady) tip splitting.

We did not carry out a detailed investigation of these instabilities since our simulations can only yield a partial view due to the influence of our specific boundary conditions. For the thin sample, our simulation box contains only a quarter of a cell, but we can capture the tip-splitting instability since it is a symmetric mode. In contrast, we cannot capture asymmetric modes which would lead to tilted or parity-broken cells. Therefore, we cannot exclude that such states could

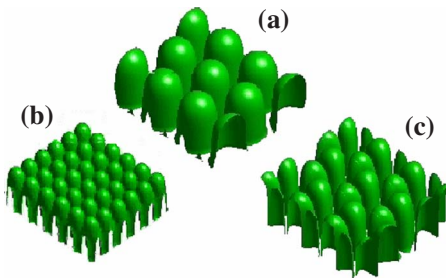


FIG. 17. (Color online) Tip splitting can involve a change of symmetry. An initially (a) hexagonal array can tip split into a (b) square symmetry or a (c) honeycomb symmetry depending on the initial wavelength. $G=38 \text{ K/cm}$ and $v_p=5.0 \mu\text{m/s}$.

exist for spacings that fall inside the “gap” reported here. Moreover, we cannot capture instabilities that involve more than one cell, such as the well-known cell elimination and oscillatory instabilities [22,29]. Therefore, the steady states found here might not all be observable in experiments. The arrays of different symmetries formed after the tip-splitting instability in Figs. 16 and 17 are stable in our simulations, but might be unstable in extended systems (we recall that the pictures are reconstructions which contain several copies of our actual simulation box). Finally, in the presence of noise, it is also expected that an instability by tertiary branching would become important for large spacings.

IV. CONCLUSIONS

We have used a computationally efficient quantitative phase-field approach to investigate three-dimensional periodic array structures formed during the directional solidification of a dilute binary alloy, focusing primarily on the dependence of steady-state growth shapes on growth rate, surface-tension anisotropy strength, and sample geometry. Furthermore, we have used our results to critically assess the quantitative predictions of existing theories for growth shapes and the tip undercooling.

We find consistently three regimes with only a finger branch of steady-state growth solutions at low velocity, separate branches of fingers and needles at intermediate velocity, and merging of those two branches into a single finger or needle branch for large velocity. Along the latter branch, the interface shape evolves continuously from finger to needle with increasing spacing. In contrast, in the intermediate-velocity range, fingers and needles exist on separate branches of steady-state growth solutions for small and large spacings, respectively. This intermediate-velocity regime agrees reasonably well quantitatively with the experimentally observed velocity regime where cells and dendrites coexist in the SCN-salol system for the same composition ($c_0=0.7 \text{ wt \% salol}$) [15].

The existence of those separate branches of fingers and needles provides a potential explanation of the characteristic jump of primary spacing observed in experiments [3,4,15] in the vicinity of the cell-to-dendrite transition (i.e., the finger-to-needle transition where needles possess sidebranches). It also accounts for the hysteretic character of this transition as a function of growth rate. In some experiments [9], however, the cell-to-dendrite transition has been observed to be continuous as a function of spacing. Our results suggest that those experiments were carried out in a velocity regime where the finger and needle branches have merged into a single branch. It should be noted that other explanations for the discontinuity in spacing have been suggested, such as a decisive role of confinement when the sample thickness becomes comparable to the cell spacing [7] or a sudden onset of the cell elimination instability for a large range of spacings with a small change in velocity [14]. Whereas our results indicate that a direct influence of the sample thickness on the transition is highly unlikely, the precise relation between the sample geometry and the cell elimination instability could only be investigated in simulations with several

cells [29], which is outside the scope of the present paper. Finally, the results of a detailed study of sidebranching including thermal noise, which sheds additional light on the cell-to-dendrite transition, will be published elsewhere [42].

We have found that the “branch structure” characterized by those three growth regimes is robust. Increasing the anisotropy strength shifts the appearance of the needle branch and its merging with the finger branch to lower velocities, but does not alter qualitatively this structure. Furthermore, interestingly, this branch structure is both qualitatively and quantitatively very similar in different three-dimensional growth geometries. Since an axisymmetric cell approximates an individual cell in a spatially extended hexagonal array, the near coincidence of branch structures, shapes, and tip undercoolings for the axisymmetric and hexagonal-array geometries is not unexpected. The near coincidence of branch structures, shapes, and tip undercoolings for those geometries and the thin-sample geometry, however, is more surprising and important in itself. It implies that computations and experiments carried out in a thin-sample geometry can be used to extract quantitative information about steady-state growth structures that would form in a spatially extended array structure in a bulk sample. The stability property of those structures, however, can generally depend on the growth geometry. The hexagonal-array structures are generally less constrained than the thin-sample array structures and can therefore exhibit a wider range of instabilities. Some tip-splitting modes were illustrated at the end of the last section, but were not systematically surveyed here.

We have used our results to critically assess the quantitative validity of the analogy between ST and solidification fingers. We find that an approximate analytical expression used to fit three-dimensional axisymmetric ST shapes [49] also fits well the finger shapes in our phase-field simulations. This analogy, however, cannot be used to predict the maximum finger spacing most likely due to the fact that solidification fingers exist on a different “diffusive” branch of growth solutions than the ST branch. This conclusion is based on previous theoretical work for bidimensional isothermal finger growth in a channel [51,52]. While a theoretical attempt has been made to extend this work to bidimensional directional solidification [21], an analytical understanding of the branch structure for directional solidification in three dimensions remains lacking.

We have also used our results to critically assess existing theories of the finger tip undercooling. We conclude that the KP theory yields more accurate predictions of the tip undercooling than the BBF theory because it accounts for solute rejection in the tip region. The KP theory, however, requires as input parameter the relative finger width that was extracted here from a fit of phase-field shapes to ST shapes. It should in principle be possible to use the same fit procedure experimentally, but an accurate measurement of the tip temperature to distinguish these theories remains a technical challenge.

We have performed our calculations for a particular set of materials parameters and ranges of control parameters motivated by the availability of experimental data [15]. While this has allowed us to understand quantitatively the influence of anisotropy and pulling speed on steady-state growth

shapes, a more exhaustive survey as a function of the various parameters (d_0/l_T , l_D/l_T , Λ/l_T , k , and ϵ) of this problem remains to be carried out. Even with the efficient phase-field model used here, such a survey remains a nontrivial computational challenge.

ACKNOWLEDGMENTS

This work was supported by NASA. M.P. also acknowledges financial support by Centre National d'Études Spatiales, France.

APPENDIX: ANISOTROPY IN THE AXISYMMETRIC PHASE-FIELD MODEL

Here, we show that the Gibbs-Thomson condition in the axisymmetric approximation, Eq. (15), can be simply obtained by simulating a phase-field model with the azimuthally averaged anisotropic surface tension given by Eq. (14) in cylindrical coordinates. Rather than giving a complete asymptotic analysis, we will outline here only the points that differ from the standard approach; the details can be worked out in a straightforward manner following the lines of previous works [37,54]. Furthermore, for simplicity, we will only consider the case of isothermal solidification.

The starting point is a dimensionless free-energy functional

$$\mathcal{F} = \int_V f(\phi, \vec{\nabla}\phi, U), \quad (\text{A1})$$

where ϕ is the phase field (with $\phi=1$ and $\phi=-1$ corresponding to the solid and the liquid, respectively), U is a dimensionless driving force (proportional to the supersaturation in the liquid), and the integral is over the full three-dimensional space. The free-energy density is of the form

$$f(\phi, \vec{\nabla}\phi, U) = \frac{1}{2}W^2(\hat{n})\vec{\nabla}\phi^2 + f_{dw}(\phi) + \lambda U g(\phi), \quad (\text{A2})$$

where $W(\hat{n})=W_0a(\hat{n})$, with W_0 the (average) interface thickness and $a(\hat{n})$ the anisotropy function defined in Eq. (5). Furthermore, $f_{dw}=-\phi^2/2+\phi^4/4$, $g(\phi)=\phi-2\phi^3/3+\phi^5/5$, and λ are the standard double-well potential, tilting function, and coupling constant used in Refs. [37,54].

To simulate this model in the axisymmetric approximation, we use the standard cylindrical coordinates, $(x, y, z) = (r \cos \varphi, r \sin \varphi, z)$, and suppose that ϕ and U are independent of φ . Furthermore, $W(\hat{n})$ is replaced by its azimuthal average, $W(\theta)=W_0\bar{a}(\theta)$. Here, θ is the angle between the unit vector perpendicular to the interface pointing into the liquid and the growth axis z given by

$$\theta = \arctan \frac{\partial_r \phi}{\partial_z \phi}. \quad (\text{A3})$$

Since f is independent of the azimuthal angle, the integral over φ can be carried out and the free-energy becomes

$$\mathcal{F} = \int 2\pi r f(\phi, \vec{\nabla}\phi, U) dr dz, \quad (\text{A4})$$

where ϕ and U are now functions of r and z only. Simulations are performed on a two-dimensional regular grid in these variables, which represents a radial slice of the axisymmetric system. The time evolution of the phase field is, as usual, given by the functional derivative of the free-energy functional. In carrying out this derivative, it has to be taken into account that the functional derivative of \mathcal{F} with respect to $\phi(r, z, t)$ represents the variation of the free energy with the change of ϕ on an entire circle of radius r ; therefore, the rate of change of a grid point located in the simulation slice is given by

$$\begin{aligned} \tau(\theta)\partial_t\phi(r, z, t) &= -\frac{1}{2\pi r} \frac{\delta\mathcal{F}}{\delta\phi(r, z, t)} \\ &= -\frac{1}{2\pi r} \left\{ 2\pi r \frac{\partial f}{\partial\phi} - \partial_z \left[2\pi r \frac{\partial f}{\partial(\partial_z\phi)} \right] \right. \\ &\quad \left. - \partial_r \left[2\pi r \frac{\partial f}{\partial(\partial_r\phi)} \right] \right\}, \quad (\text{A5}) \end{aligned}$$

where $\tau(\theta)$ is the (orientation-dependent) relaxation time of the phase field. It can be seen that the factors $2\pi r$ cancel out from the first two terms, which become thus identical to the ones that would have been obtained in a standard Cartesian coordinate system. Furthermore, the last term gives rise to two contributions. When the partial derivative ∂_r acts on the derivative of f , the factors $2\pi r$ again cancel out. Together with the first two terms, this contribution constitutes an expression which is identical to the functional derivative of an anisotropic free energy in two dimensions. This results, in the sharp-interface limit, in the term proportional to $A(\theta)$ in

Eq. (14); indeed, $\bar{a} + d^2\bar{a}/d\theta^2$ and R_1 are just the stiffness and radius of curvature in the (r, z) plane, respectively. The only contribution that is specific to the axisymmetric situation is therefore the terms that result from the action of ∂_r on r itself. These new terms are

$$\frac{1}{r} \frac{\partial f}{\partial(\partial_r\phi)} = \frac{W_0^2 \bar{a}}{r} \left[\bar{a} \partial_r \phi + \frac{d\bar{a}}{d\theta} \frac{\partial\theta}{\partial(\partial_r\phi)} \right]. \quad (\text{A6})$$

Equation (A3) yields $\partial\theta/\partial(\partial_r\phi) = \cot\theta \partial_r\phi$. Furthermore, in the limit where the radii of curvature are much larger than the interface thickness, we can consider that θ varies only weakly across the diffuse interface and is approximately given by $\tan\theta = -z'(r)$, where $z(r)$ is the interface shape in the sharp-interface representation. Then, $\partial_r\phi = \sin\theta \partial_n\phi = -z'/\sqrt{1+z'^2} \partial_n\phi$, where $\partial_n\phi$ is the derivative along the interface normal. In this limit, the additional terms become hence

$$\frac{1}{r} \frac{\partial f}{\partial(\partial_r\phi)} = \frac{W_0^2 \bar{a}}{R_2} \left[\bar{a} + \cot\theta \frac{d\bar{a}}{d\theta} \right] \partial_n\phi, \quad (\text{A7})$$

with R_2 given by Eq. (18). Up to the factor in large brackets, this is of the same form as the standard curvature correction in an isotropic phase-field model. Therefore, it is straightforward to show that, in the sharp-interface limit, this contribution yields the terms proportional to $B(\theta)$ in Eq. (14).

The analysis of the kinetic effects is not modified by the change of coordinates; therefore, local equilibrium at the interfaces can be obtained, as in Ref. [54], by appropriately choosing $\tau(\theta) \sim a(\theta)^2$. Equation (A5) is then simulated together with the evolution equation for U , in which the divergence operators are replaced by the appropriate expression in cylindrical coordinates. Note that there is no singularity for $r \rightarrow 0$ since $r=0$ is a symmetry axis and hence we impose vanishing derivatives of all fields in $r=0$.

[1] W. Kurz and D. J. Fisher, *Fundamentals of Solidification* (Trans Tech, Aedermannsdorf, Switzerland, 1992).
 [2] J. A. Dantzig and M. Rappaz, *Solidification* (EPFL Press, Lausanne, Switzerland, 2009).
 [3] V. Seetharaman and R. Trivedi, *Metall. Trans. A* **19**, 295 (1988); M. A. Eshelman, V. Seetharaman, and R. Trivedi, *Acta Metall.* **36**, 1165 (1988); V. Seetharaman, M. A. Eshelman, and R. Trivedi, *ibid.* **36**, 1175 (1988).
 [4] P. Kurowski, C. Guthmann, and S. de Cheveigné, *Phys. Rev. A* **42**, 7368 (1990).
 [5] H. Jamgotchian, R. Trivedi, and B. Billia, *Phys. Rev. E* **47**, 4313 (1993).
 [6] S. Akamatsu, G. Faivre, and T. Ihle, *Phys. Rev. E* **51**, 4751 (1995).
 [7] B. Billia, H. Jamgotchian, and H. Nguyen-Thi, *J. Cryst. Growth* **167**, 265 (1996).
 [8] M. Georgelin and A. Pocheau, *Phys. Rev. Lett.* **79**, 2698 (1997).
 [9] M. Georgelin and A. Pocheau, *Phys. Rev. E* **57**, 3189 (1998).
 [10] S. Akamatsu and G. Faivre, *Phys. Rev. E* **58**, 3302 (1998).
 [11] W. Losert, D. A. Stillman, H. Z. Cummins, P. Koczynski, W.-J. Rappel, and A. Karma, *Phys. Rev. E* **58**, 7492 (1998).
 [12] A. Pocheau and M. Georgelin, *J. Cryst. Growth* **206**, 215 (1999).
 [13] B. Utter, R. Ragnarsson, and E. Bodenschatz, *Phys. Rev. Lett.* **86**, 4604 (2001).
 [14] A. Pocheau and M. Georgelin, *J. Cryst. Growth* **250**, 100 (2003).
 [15] R. Trivedi, S. Yunxue, and S. Liu, *Metall. Mater. Trans. A* **34**, 395 (2003).
 [16] L. H. Ungar and R. A. Brown, *Phys. Rev. B* **31**, 5931 (1985).
 [17] A. Karma and P. Pelcé, *Phys. Rev. A* **39**, 4162 (1989).
 [18] D. A. Kessler and H. Levine, *Phys. Rev. A* **39**, 3041 (1989).
 [19] Y. Saito, C. Misbah, and H. Müller-Krumbhaar, *Phys. Rev. Lett.* **63**, 2377 (1989).
 [20] J. D. Weeks, W. van Saarloos, and M. Grant, *J. Cryst. Growth* **112**, 244 (1991).
 [21] E. A. Brener and D. E. Temkin, *Sov. Phys. JETP* **82**, 559 (1996).
 [22] P. Koczynski, W.-J. Rappel, and A. Karma, *Phys. Rev. Lett.* **77**, 3387 (1996).
 [23] P. Koczynski, W.-J. Rappel, and A. Karma, *Phys. Rev. E* **55**,

- R1282 (1997).
- [24] N. Provatas, Q. Wang, M. Haataja, and M. Grant, Phys. Rev. Lett. **91**, 155502 (2003).
- [25] M. Greenwood, M. Haataja, and N. Provatas, Phys. Rev. Lett. **93**, 246101 (2004).
- [26] G. B. McFadden, R. F. Boisvert, and S. R. Coriell, J. Cryst. Growth **84**, 371 (1987).
- [27] B. Grossmann, K. R. Elder, M. Grant, and J. M. Kosterlitz, Phys. Rev. Lett. **71**, 3323 (1993).
- [28] J. D. Hunt and S.-Z. Lu, Metall. Mater. Trans. A **27**, 611 (1996).
- [29] M. Plapp and M. Dejmek, Europhys. Lett. **65**, 276 (2004).
- [30] B. P. Athreya, J. A. Dantzig, S. Liu, and R. Trivedi, Philos. Mag. **86**, 3739 (2006).
- [31] E. Meca and M. Plapp, Metall. Mater. Trans. A **38**, 1407 (2007).
- [32] M. Plapp and A. Karma, Phys. Rev. Lett. **84**, 1740 (2000).
- [33] A. Karma, Y. H. Lee, and M. Plapp, Phys. Rev. E **61**, 3996 (2000).
- [34] J. H. Jeong, J. A. Dantzig, and N. Goldenfeld, Metall. Mater. Trans. A **34**, 459 (2003).
- [35] Y. Lu, C. Beckermann, and J. C. Ramirez, J. Cryst. Growth **280**, 320 (2005).
- [36] A. Karma, Phys. Rev. Lett. **87**, 115701 (2001).
- [37] B. Echebarria, R. Folch, A. Karma, and M. Plapp, Phys. Rev. E **70**, 061604 (2004).
- [38] M. N. Barber, A. Barbieri, and J. S. Langer, Phys. Rev. A **36**, 3340 (1987).
- [39] E. Brener and D. E. Temkin, Phys. Rev. E **51**, 351 (1995).
- [40] U. Bisang and J. H. Bilgram, Phys. Rev. E **54**, 5309 (1996).
- [41] A. Karma and W.-J. Rappel, Phys. Rev. E **60**, 3614 (1999).
- [42] B. Echebarria, A. Karma, and S. Gurevich (unpublished).
- [43] P. G. Saffman and G. I. Taylor, Proc. R. Soc. London, Ser. A **245**, 312 (1958); for a review see D. Bensimon, L. Kadanoff, S. Liang, B. I. Shraiman, and L. Tang, Rev. Mod. Phys. **58**, 977 (1986).
- [44] J. S. Langer, in *Chance and Matter*, Proceedings of the Les Houches Summer School of Theoretical Physics, Session XLVI, Les Houches, 1986, edited by J. Souletie, J. Vannimenus, and R. Stora (North Holland, Amsterdam, 1987), p. 629.
- [45] T. F. Bower, H. D. Brody, and M. C. Flemings, Trans. Metall. Soc. AIME **236**, 624 (1966).
- [46] A. Barbieri and J. S. Langer, Phys. Rev. A **39**, 5314 (1989).
- [47] W. J. Boettinger, J. A. Warren, C. Beckermann, and A. Karma, Annu. Rev. Mater. Res. **32**, 163 (2002).
- [48] R. Folch and M. Plapp, Phys. Rev. E **72**, 011602 (2005).
- [49] H. Levine and Y. Tu, Phys. Rev. A **45**, 1044 (1992).
- [50] R. Trivedi, R. S. Liu, B. Echebarria, and A. Karma, *Solidification Processes and Microstructures* (The Minerals, Metals and Materials Society, Warrendale, PA, 2004), pp. 307–318.
- [51] E. A. Brener, M. B. Geilikman, and D. E. Temkin, Zh. Eksp. Teor. Fiz. **94**, 241 (1988).
- [52] E. A. Brener, H. Müller-Krumbhaar, Y. Saito, and D. E. Temkin, Phys. Rev. E **47**, 1151 (1993).
- [53] P. Koczynski, Ph.D. thesis, Northeastern University, 1998.
- [54] A. Karma and W.-J. Rappel, Phys. Rev. E **57**, 4323 (1998).